Transformation of Hydrogel-Based Inverse Opal Photonic Sensors from FCC to L1₁ during Swelling

Yun-Ju Lee,[†,§] **Carla E. Heitzman,**[†] **Walter R. Frei,**[‡] **H. T. Johnson,**[‡] **and Paul V. Braun*,**[†]

Department of Materials Science and Engineering, Beckman Institute for Advanced Science and Technology, and Frederick Seitz Materials Research Laboratory, and Department of Mechanical Science and Engineering, University of Illinois at Urbana-Champaign, Urbana, Illinois 61801

Received: June 20, 2006

The structural evolution of Bragg diffracting inverse opal hydrogel sensors during swelling is directly observed by two-photon laser scanning fluorescence microscopy and compared to predictions from finite element analysis. A fluorescently labeled pH-sensitive hydrogel is UV-polymerized in a dried polystyrene colloidal crystal template, which is etched to yield an inverse opal. Fluorescence imaging of the hydrogel at different pH values reveals an inhomogeneous deformation of the FCC array of aqueous pores. The pores elongate along the sample normal direction and collapse along the sample parallel directions, consistent with the Bragg response, which indicates a 1-D increase in the interlayer distance. Interconnects between the pores serve as anchor points during hydrogel expansion into the pores. Pinning of the hydrogel to the substrate causes a change of the hydrogel lattice symmetry during deformation, from FCC (ABC stacking) to L1₁ (ABCA′B′C′ stacking). Reconstructed cross-sections confirm that a 1-D increase in the interlayer distance along the substrate normal direction is responsible for the diffraction response of an inverse opal hydrogel sensor. Comparison with predictions from finite element analysis shows qualitative agreement, although the experimental mesostructure is significantly more deformed than the calculated data, due to buckling in the experimental system that is not captured by the model.

Introduction

3-D periodically ordered mesostructures formed from functionalized hydrogels are increasingly utilized as chemical and biological sensors with tunable Bragg diffraction.[1–16] These mesostructures are created through templating with self-assembled colloidal crystals (CCs) formed using techniques including charge stabilization,[17–19] sedimentation on patterned substrates,[20,21] convective self-assembly,[22–25] and sonication assisted packing.[26] Following colloidal assembly, responsive materials, such as hydrogels, are then introduced in the space between the colloidal particles. Because of the periodic structure, even at small refractive index contrast, an incomplete photonic gap develops where certain frequencies of light are forbidden from propagating in the material at specific directions. Such a partial gap manifests itself as a Bragg diffraction peak; for a periodically ordered material with a face-centered cubic (FCC) structure where the (111) planes lie parallel to the substrate, the first-order Bragg diffraction wavelength, λ_b, can be estimated as:

$$\lambda_b = \frac{2\sqrt{3}}{3}\left(\sum_i n_i^2 \phi_i - \sin^2 \psi\right)^{1/2} a \qquad (1)$$

where n_i and ϕ_i are, respectively, the refractive index and the volume fraction of each component phase, ψ is the angle between the incident beam and the sample normal, and a is the FCC lattice constant.[27] For touching spheres with diameter D, $a = \sqrt{2}D$.

The incorporation of hydrogels in CC templates represents a facile method for fabricating optically responsive mesostructured sensors, because functionalized hydrogels can undergo reversible volumetric changes when exposed to stimuli such as solvent composition,[28,29] temperature,[30,31] pH and ionic strength,[32] and biomolecule binding.[33–36] By imparting the periodicity of the CC template to the infiltrated hydrogel, the response to stimuli may cause a change in a, n, and/or ϕ, leading to a shift in λ_b. Using CC templating followed by template etching, we and others have analyzed the response of inverse opal hydrogel Bragg diffractive sensors to temperature,[12,13] pH and ionic strength,[14] relative humidity,[16] and biomolecules.[15,37] While examining the Bragg response of these mesostructures, we notice several interesting trends in the swelling behavior of these hydrogel sensors. First, as λ_b red shifts due to hydrogel swelling, the diffraction peak intensity, I_b, monotonically decreases.[14,15] When compared to analytical predictions using a scalar wave approximation method,[38] we find the result to be qualitatively consistent with a decrease in the volume fraction of the FCC pores and/or an increase in disorder during hydrogel swelling.[15] Second, the relative magnitude of the diffraction shift $\Delta\lambda_b/\lambda_{b0}$ at various analyte concentrations (where λ_{b0} is the diffraction wavelength of the hydrogel in the compact state) appears to be linearly proportional to the concentration of the functional group.[14,15] Because our reflectance spectrometer probes dimensional changes in the sample normal direction,[15] the linear concentration dependence implies that the hydrogel swelling is limited to the FCC[111] direction. In this report, we directly

* Corresponding author. Phone: (217) 244-7293. Fax: (217) 333-2736. E-mail: pbraun@uiuc.edu.
† Department of Materials Science and Engineering, Beckman Institute for Advanced Science and Technology, and Frederick Seitz Materials Research Laboratory.
‡ Department of Mechanical Science and Engineering.
§ Current address: Sandia National Laboratories, P.O. Box 5800, MS 1082, Albuquerque, NM 87185.

image a Rhodamine B (RhoB)-labeled inverse opal hydrogel pH sensor using two-photon laser scanning fluorescence microscopy to characterize the mesostructure evolution of inverse opal hydrogel sensors during swelling. Along with the expected swelling normal to the substrate, we find that the templated inverse opal structure undergoes a number of unique structural transformations upon swelling, including a transformation from FCC to an $L1_1$-like crystal structure.

Multiphoton excitation of fluorophors is an attractive technique for studying submicrometer 3-D structures and processes because of the potential for high-resolution imaging.[39,40] 2-D cross-section images are collected, from which 3-D structures can be reconstructed. For example, the microstructure of poly-(vinyl alcohol) hydrogels formed by freezing-induced phase separation was recently examined by two-photon fluorescence microscopy.[41] In addition, through multiphoton imaging, photobleaching of the fluorophor and scattering due to the refractive index contrast between the hydrogel ($n = 1.51$) and the aqueous solvent ($n = 1.33$) are minimized.[42] RhoB is often utilized in multiphoton imaging, because it exhibits a good two-photon cross-section at 780 nm,[40,43] and its fluorescence is not strongly affected by pH. Thus, the hydrogel mesostructure as a function of pH can be studied in detail.

Using two-photon excitation, fluorescence cross-sections of a carboxylic acid-functionalized inverse opal hydrogel in pH buffers ranging from 3 to 7 are collected. The mesostructure of the hydrogel at different swelling ratios is reconstructed from the images via software to examine the evolution of the FCC pore morphology during hydrogel swelling. Changes in the characteristic distance between layers of pores at different pH are compared to the Bragg diffraction response of another hydrogel fabricated with a smaller diameter colloidal template to determine the relative contributions of n and d to eq 1. Finally, the experimental data are compared to analytical predictions from finite element modeling.

Experimental Section

Materials. Aqueous suspensions of monodisperse polystyrene colloids (1-200, batch 1389,1, $D = 244 \pm 7$ nm and 2-3000, batch 296B, $D = 3 \pm 0.087$ μm) were purchased from Interfacial Dynamics Co., Portland, OR. 2-Hydroxyethyl methacrylate (HEMA) (Sigma-Aldrich), acrylic acid (AA) (Acros), ethylene glycol dimethacrylate (EGDM) (Sigma-Aldrich), Irgacure 651 photoinitiator (IR-651) (Ciba Specialty Chemicals), octadecyltrichlorosilane (OTS) (Acros), methacryloxypropyltrimethoxysilane (MPMS) (Gelest, Inc., Tullytown, PA), Rhodamine B isothiocyanate (RhoB-ITC) (Sigma-Aldrich), 2-aminoethyl methacrylate hydrochloride (AEMA) (Acros), citric acid (Acros), and K_2HPO_4 (Acros) were used as received. 48-gauge Mylar LBT films (12 μm) were donated by Dupont Teijin Films. Milli-Q deionized water (Millipore) was used for all experiments. All pH measurements were taken using an Accumet AR-10 pH meter (Fisher Scientific). Samples were sonicated on a Fisher F530 sonicator (Fisher Scientific).

Colloidal Template Formation. Our procedure for forming CCs[15] was based on sonication-assisted packing[26] and was used to fabricate CC templates ($D = 244$ nm) on 25 mm × 25 mm glass slides. A second set of CC templates with larger diameter colloids ($D = 3$ μm) were formed using the same procedure on 22 mm × 22 mm cover slips (No. 1, Corning), which was placed on top of a similarly sized Mylar film and a glass slide to prevent it from cracking when clamped during flow cell assembly. All glass surfaces were treated with either OTS or MPMS to ensure that the hydrogel was attached to the bottom substrate after

polymerization. After being sonicated for ~24 h, the CC templates were dried by exposure to air through the empty reservoir for 24 h.

Acrylated RhoB Synthesis. RhoB-ITC (9.4 mg, 17.5 μmol) and AEMA (2.9 mg, 17.5 μmol) were dissolved in water (1.75 mL), and the pH was adjusted to ~6 by adding 1 M NaOH (aq) (~50 μL). The solution was stirred for 2 h at room temperature to complete the reaction and was used without further purification.

Inverse Opal Hydrogel Synthesis. The fabrication procedure for inverse opal hydrogels has been reported previously[15] and was used here with the following modifications. A pH-sensitive monomer mixture was formed by dissolving AA (13.9 mg, 193 μmol), EGDM (5.0 mg, 25.2 μmol), and IR-651 (10.5 mg, 40.3 μmol) in HEMA (0.471 g, 3.62 mmol). For the fluorescent mixture, 1 μL of the RhoB solution (10 mM) was diluted with 10 μL of the monomer mixture; 4 μL of the resulting product was then mixed with 400 μL of the monomer mixture to yield a RhoB concentration of ~10 μM. Next, ~300 μL of either standard or fluorescent monomer mixture was pipetted into the reservoir above the appropriate CC template ($D = 244$ nm for microspectroscopy, $D = 3$ μm for fluorescence microscopy) and then capped with a rubber bulb. Following successful infiltration and removal of excess precursor, the hydrogel was photopolymerized at 365 nm for 50 min using a high-intensity UV lamp (B-100A, UVP, Inc., Upland, CA). Each bottom substrate containing the hydrogel was placed in $CHCl_3$ for at least 24 h to dissolve the CC template, transferred to ethanol and then to water, and finally placed in 1 mM HCl (aq) for storage.

Microspectroscopy of Hydrogel Response. The microspectrometer consisted of an inverted optical microscope (Axiovert 135, Carl Zeiss Inc.) fiberoptically coupled to a diffraction grating photodiode array detector (PDA-512, Control Development, Inc., South Bend, IN) to collect the reflectance spectra in the sample normal direction. The 400 μm diameter of the optical fiber limited the microspectroscopy analysis area to a circular spot ~16 μm in diameter.

10 mM pH buffer solutions with ionic strength (I) of 0.15 M were prepared in the following manner. Solutions of 1 M citric acid (aq) and 2 M K_2HPO_4 (aq) were prepared. Appropriate amounts of two solutions were added to KCl and diluted with water to make buffers with pH values ranging from 2 to 8, following published recipes.[44] For example, 1 M citric acid (277 μL), 2 M K_2HPO_4 (723 μL), and KCl (847 mg, 11.4 mmol) were diluted with water (98.5 mL) to make 100 mL of a pH ~6.5 buffer with $I = 0.15$ M. The pH value of each buffer was confirmed with a pH meter. Collection of the normal incidence reflectance spectra for the inverse opal hydrogel at different pH followed the reported method.[14] Briefly, the hydrogel/substrate slide was placed in a Petri dish on top of the inverted reflection microscope and submerged in 10 mL of a pH 2 buffer. The light was focused through a 10× objective onto the sample, and the reflectance was collected over an integration time of 1 s. The pH was changed by replacing about one-half of the solution with a different pH buffer. The resulting pH was measured, and the reflectance data were collected after equilibration, with pH ranging from 3.5 to 7. All spectra were normalized to 100% reflectance (front silvered mirror) and 0% reflectance. λ_b was determined by subtracting a constant background from each normalized reflectance spectra and finding the wavelength corresponding to the maximum reflectance.

Two-Photon Fluorescence Microscopy. The mesostructure of a RhoB-labeled inverse opal hydrogel sensor was imaged by two-photon fluorescence microscopy using a laser scanning confocal microscope (LSCM) (SP2, Leica). The excitation source was a mode locked Ti:sapphire laser at 780 nm (Spectra-Physics). A $63\times$ oil immersion objective collected the reflectance and fluorescence signal from the hydrogel encased in a custom imaging flow cell. First, the hydrogel/substrate was placed on an aluminum disk with a hole machined in the center to allow for imaging with the oil immersion objective through the cover slip. A Viton O-ring (OD $\approx$ 20 mm) was placed on top of the sample to act as a gasket, and a machined polycarbonate piece was placed above the O-ring and secured to the aluminum substrate via through screws to seal the flow cell. pH buffers were introduced into the cell via two Luer lock adapters through the top of the polycarbonate piece. Once the flow cell was placed on top of the mechanized translation/tilt stage of the LSCM, the sample was aligned so that it rested in a horizontal position, and the image was focused at the hydrogel/cover slip interface using the reflectance mode of the LSCM. For fluorescence scans, a diffraction grating monochromator limited the collection wavelength range from 550 to 700 nm. Laser intensity was adjusted to obtain good image contrast while minimizing photobleaching and thermal damage. A series of horizontal scans with 1024 × 1024 pixels were performed with a full field view of 60 μm × 60 μm. Each horizontal scan was separated by a vertical displacement of 203.5 nm. Thus, the raw 3-D voxel size was 58.5 nm × 58.5 nm × 203.5 nm. The orientation of the horizontal scans corresponded to the imaging of FCC(111) planes. pH was adjusted by flushing the cell with an excess of the new buffer, and the resulting pH was determined by measuring the effluent pH. The imaging procedure was repeated at three additional pH values. Cross-sections along other crystallographic orientations were reconstructed via software (Analyze, Mayo Clinic). From the vertical cross-sections, the characteristic interlayer distance d for each pH was determined and compared to the characteristic distance d_0 when the hydrogel was in its most compact state.

Finite Element Modeling of Mesostructure Deformation. A hexahedral mesh with a maximum element size of 30 nm was applied to an inverse opal structure representing the hydrogel. Although hexahedral elements introduce topologic aliasing, they exhibit much improved numerical performance as compared to tetrahedral elements for large-deformation geometric nonlinear analysis, and therefore were used. The symmetry of the inverse opal structure was exploited, and an irreducible triangular prismatic unit cell model was created, with three layers of pores, representing the ABC stacking of the FCC-(111) planes. To approximate the real structure of the colloidal template (slight sintering at the contact points), spherical FCC voids with a center-to-center distance of 125/128 of the diameter of the voids were used. The Arruda−Boyce material model[45] was utilized because only uniaxial tensile test data were available. The pH-dependent mechanical properties of the AA-functionalized hydrogel were adapted from the literature.[46] Symmetry boundary conditions were applied to the sides of the triangular prism, while the hydrogel/substrate interface was fixed. A uniform bulk strain corresponding to the observed vertical strain was applied to the mesh by applying a thermal strain to the entire model to determine the equilibrium pore mesostructure of the hydrogel. The ABAQUS/Standard geometric nonlinear solver was used to solve the finite element model. To qualitatively approximate the collection of fluorescence signal from the hydrogel at various points within the laser
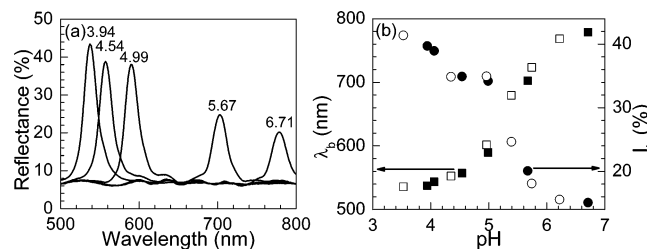
Figure 1. (a) Reflectance spectra of a 5% AA hydrogel at selected pH. (b) λ_b (squares) and I_b (circles) of a 5% AA hydrogel as a function of pH. Filled symbols, increasing pH; open symbols, decreasing pH.

focal volume, cross-sections separated by a distance of $D/12$ were obtained from the finite element result, the intensity of each pixel was arithmetically averaged using Adobe Photoshop, and finally the image was blurred using an $\sim$250 nm (8 pixel) Gaussian blur. This procedure simulated the focal volume collected on the microscope. For the FCC(111) cross-sections, images from $\pm D/3$ (where zero corresponds to a cross-section through the center of a pore) were averaged; for the FCC(-110) cross-sections, images from $\pm D/4$ were averaged.

A coarse-grained finite element model with an $\sim$30 nm mesh size was used to model the hydrogel deformation for several reasons. This mesh size was $\sim$10 times smaller than the resolution of the two-photon microscopy, and thus a smaller mesh would not yield additional information that could be compared to the experimental data. Also, further reductions in the mesh size cause the finite element calculations to terminate at smaller bulk strain as the ligaments near interconnects began to overlap each other, creating numerical singularities. Because the interconnect regions contribute minimally on the overall deformed shape, the loss of resolution for localized deformations does not impact the overall analysis.

Results and Discussion

Diffraction Response. The reflectance spectra of the 5% AA hydrogel at different pH values are shown in Figure 1a. At pH < 4, the Bragg diffraction is consistent with the expected response from an undeformed inverse FCC structure of polymer ($n = 1.51$) in water ($n = 1.33$), with $\lambda_{b0} = 537$ nm. When pH is increased, the peak steadily red shifts reaching $\lambda_b = 779$ nm at pH = 6.71 (Figure 1b). By allowing sufficient time to elapse after a pH change ($\sim$30 min), the hysteresis in λ_b for increasing versus decreasing pH becomes very small (Figure 1b, squares). We also observe a reversible attenuation of I_b during the pH increase (from 39.7% to 15.1%), which seems to strongly correlate to the diffraction shift, and therefore to hydrogel swelling (Figure 1b, circles). The characteristics of the diffraction trend as a function of hydrogel swelling closely match the data from our earlier reports.[14,15]

Imaging of Hydrogel Mesostructure Deformation. The fluorescence cross-section images illustrate the dramatic change in pore morphology as pH increases and the inverse opal hydrogel swells. For example, the FCC(111) cross-sections for layers not adjacent to the hydrogel/substrate interface show significant pore shrinkage and deformation as the pH increases from 3.4 to 6.6 (Figure 2a). After hydrogel swelling, the darker regions, corresponding to the water filled pores, account for a smaller fraction of the total image area. In addition, a typical pore cross-section deforms from a slightly distorted circle at pH = 3.5 to a triangle at pH = 5.0 and finally to a three-pointed star by pH = 6.6 (Figure 2a). Closer examination reveals that the endpoints of each three-pointed star in the swollen hydrogel occupy the same spatial position as the interconnects between
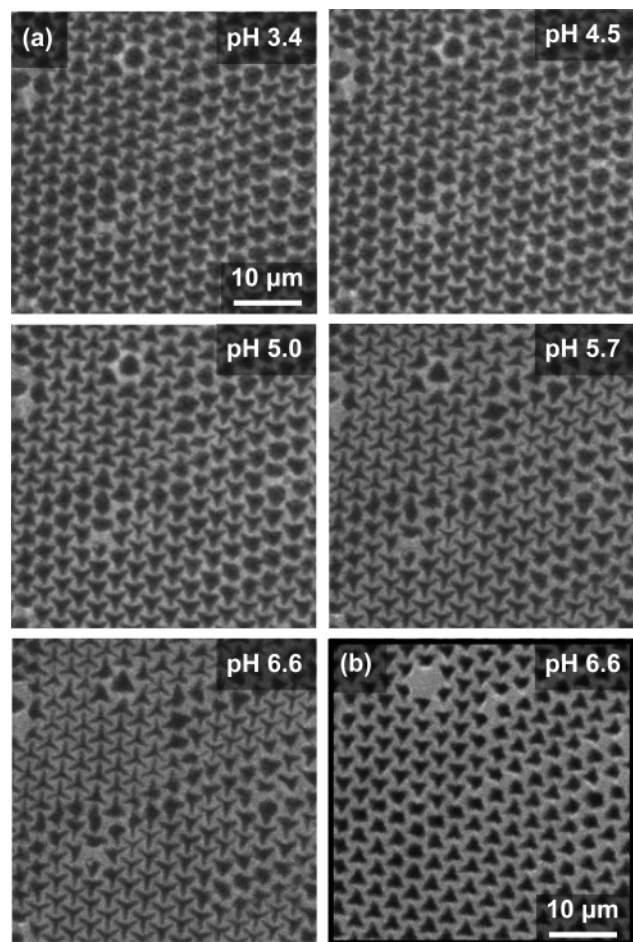
Figure 2. (a) FCC(111) cross-sections of the hydrogel for the second layer above the hydrogel/cover slip interface at varying pH. (b) FCC-(111) cross-section of the hydrogel for the first layer at pH = 6.6.

each pore and its nearest neighbors in the compact hydrogel. The interconnects appear to stay on a close-packed lattice, while the rest of the hydrogel expands. Such behavior is reasonable considering that, in an inverse opal structure, the material closest to the interconnects is thin and should exhibit a smaller absolute deformation as compared to thicker elements. As we show later, this behavior is also observed in the finite element modeling results. The FCC(111) cross-section for the layer closest to the interface, which is pinned to the noncompliant glass substrate through covalent linkages, exhibits significantly less pore deformation as the pH increases as compared to the overlying layers; at pH = 6.6, the cross-section of the first layer is triangular, but not star-shaped (Figure 2b). As shown by our previous predictions,[15] the observed pore shrinkage in an expanding inverse opal hydrogel is consistent with the peak attenuation in the reflectance spectra.

The fluorescence cross-sections of the pore deformation suggest that a change in the crystallographic symmetry of the inverse opal structure occurs during hydrogel expansion. Specifically, the orientation of the triangles in each layer of deformed pores is rotated 180° as compared to the adjacent layers (Figure 3a). The alternation of pore orientation in a swollen hydrogel may correspond to a transformation of the aqueous pores from ABCABC stacking (FCC) to ABCA′B′C′ stacking (L1$_1$ lattice). We believe that this lattice transformation can be explained by the spatial distribution of strain within a swollen hydrogel (schematically illustrated in Figure 3b). As the hydrogel swells, the L1$_1$ pore symmetry allows the surrounding hydrogel to

deform more uniformly, as shown by the more uniform thickness of the hydrogel (white) located between the first layer (blue) and second layer (red), and also between the second layer and third layer (green) (Figure 3b). For the pores to maintain a FCC symmetry, the connecting hydrogel elements would be highly strained, as shown by their triangular cross-section (Figure 2b). Because a uniform deformation is more stable, the L1$_1$ pore symmetry is favored for a deformed inverse opal hydrogel at equilibrium.

The fluorescence cross-sections exhibit other interesting features, which may help explain the previously observed trends in the Bragg diffraction peak shape. For example, the fluorescence cross-sections reveal that disorder becomes more prominent as the mesostructured hydrogel swells. At pH = 6.6, more than one-half of the pores in a 5% AA hydrogel two layers away from the hydrogel/substrate interface exhibit random cross-sections (Figure 4a), possibly caused by local buckling of the surrounding hydrogel. In addition, the irregularly shaped pores appear with greater frequency near defects and drying cracks of the original CC template (Figure 4a). Such inhomogeneous deformations may be caused by the excess hydrogel present near the defects. Fluorescence cross-sections also reveal that the highly swollen hydrogel contains domains with alternating pore orientations within the same FCC(111) layer, and excess hydrogels that infiltrated line defects in the CC template may act as the domain boundaries (Figure 4b). These boundaries may be analogous to the domain walls and/or antiphase boundaries observed in certain alloys and ferroelectric materials.[47−50] Thus, defects formed during initial CC assembly can impact the Bragg diffraction response of the resulting inverse opal hydrogel, by amplifying different types of disorder during hydrogel expansion, and by acting as domain boundaries that control the orientation of the pores in a swollen hydrogel.

Through software reconstruction, the mesostructure evolution of the swelling hydrogel can be examined in other crystallographic directions. Figure 5a shows FCC(−110) cross-sections of the inverse opal hydrogel. At pH = 3.4, the spherical pores exhibit the expected ABC stacking. As pH increases, the deformation of the surrounding hydrogel causes the pores to adopt a complex shape, consisting of an elliptical cross-section with two narrow extensions at the upper right and lower left corners (Figure 5a). The eccentricity of the ellipse increases at higher pH, corresponding to increasing d in the sample normal direction and pore shrinkage in the sample parallel directions. At the same time, the extensions exhibit only minor changes in their shape and orientations, thus maintaining the connectivity between layers of pores. Finally, the depth resolution of the fluorescence images improves at higher pH, due the reduction in scattering as the refractive index of the swollen hydrogel approaches that of water.

To calculate d/d_0 from fluorescence microscopy data, we measure the distance between neighboring FCC (−110) layers, $d(-110)$, from Figure 5a and normalize it to the value at pH = 3.4, $d(-110)_0$. It should be noted that $d(-110)_0$ should be equal to D, as confirmed by $d(-110)$ at pH = 3.4, which is 3.0 μm. After normalization, the ratios calculated from the fluorescence data are compared to λ/λ_0 from microspectroscopy. When plotted as a function of pH, both sets of data overlap within experimental error (Figure 5b), suggesting that the increase in interlayer distance in the sample normal direction completely accounts for the Bragg diffraction response of inverse opal hydrogels. Also, we compare $d(-110)/d(-110)_0$ from the fluorescence images to the change in diameter of cylindrical pH-sensitive hydrogels polymerized inside capillary tubes and
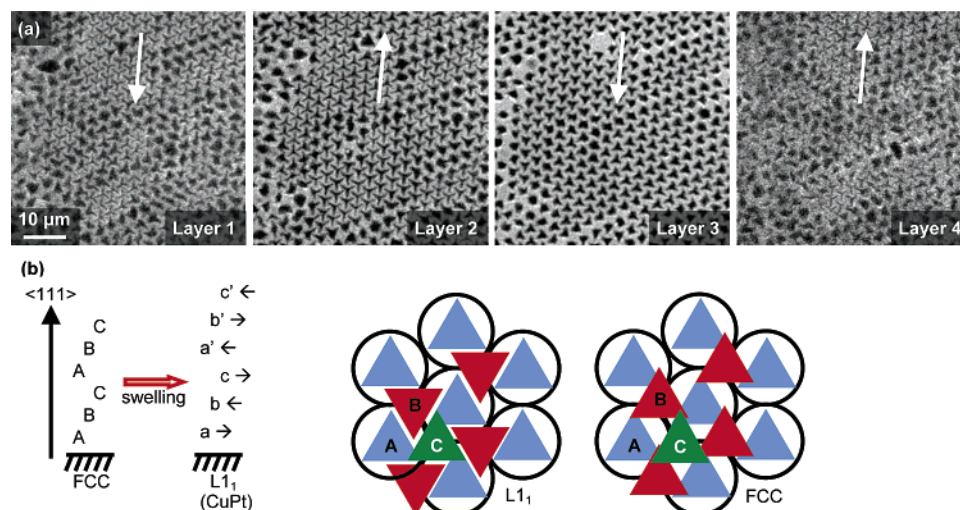
Figure 3. (a) FCC(111) cross-sections of the swollen hydrogel at pH 6.6 at increasing layer numbers above the substrate, showing an alternating pore orientation. (b) Schematic of crystallographic transformation from FCC to $L1_1$ (CuPt) symmetry.
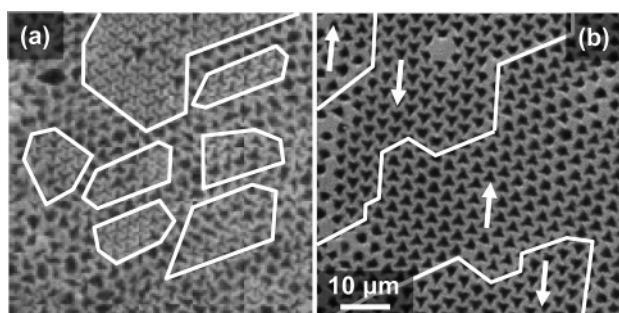

Figure 4. (a) Two-photon fluorescence microscopy reveals the increasing predominance of defects in a highly swollen hydrogel (pH = 6.6, layer 3). (b) Domain walls also became visible in a highly swollen hydrogel (pH = 6.6, layer 1).
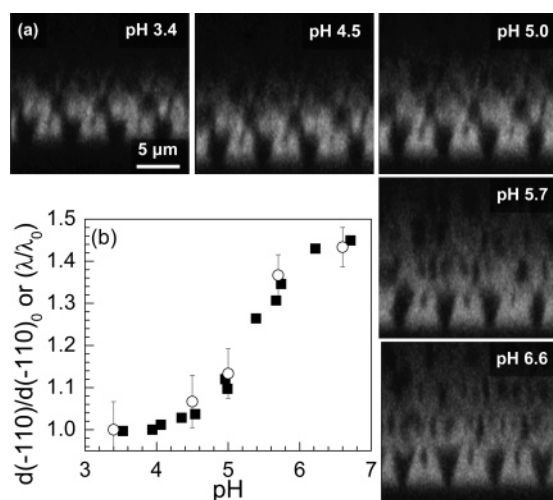
Figure 5. (a) Reconstructed FCC(-110) cross-section of the hydrogel at different pHs. (b) pH dependence of normalized $d(-110)$ from confocal (○) and normalized diffraction shift (λ_b/λ_{b0}) (■), showing essentially identical trends.

find that the inverse opal hydrogels swelled less than the solid cylindrical samples (data not shown), suggesting that inverse opal hydrogels expand both in the sample normal direction and into the pores.

Finite Element Modeling. Applying a thermal expansive bulk strain to the inverse opal hydrogel mesh and constraining the model to only expand in the substrate normal direction
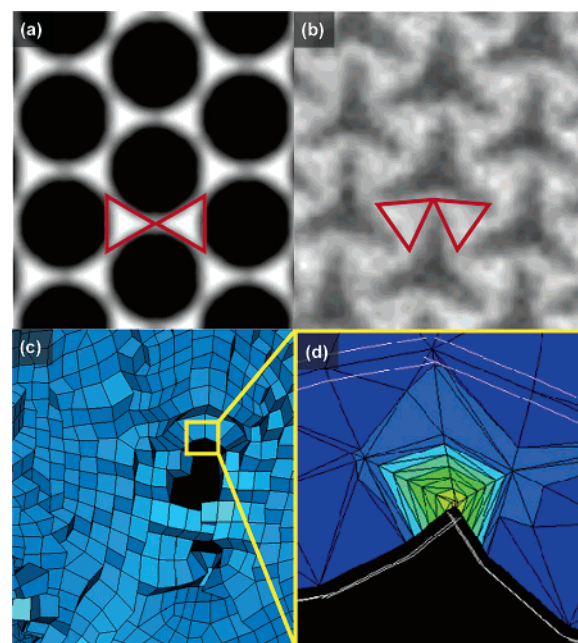
Figure 6. (a) Average of FCC(111) finite element cross-sections between $\pm D/3$ of the center of a pore. (b) FCC(111) fluorescence image of hydrogel inverse opal (pore center-to-center spacing 3 μm). Both (a) and (b) have similar strain in the sample normal direction. The red triangles highlight the buckling in the experimental sample, and lack of buckling in the model. (c) View of the finite element mesh looking approximately normal to the plane of the hole between two voids at intermediate mesh deformation. (d) Close-up view of the top of the hole between the voids showing a very high local deformation. Blue, low strain; yellow, greatest strain.

results in a pore mesostructure that captures some, but not all, of the deformations observed in the fluorescence images. At a uniform thermal expansion necessary to generate a strain of 0.3 in the sample normal direction, the FCC(111) cross-section from finite element modeling exhibits circular pore cross-sections even after averaging the data from different focal depths (Figure 6a). When compared to a high magnification image of the inverse opal hydrogel at similar strain (Figure 6b), it becomes very clear that the finite element model is not capturing the buckling observed in the experimental system. Two of the buckled regions in the (111) cross-section are outlined in red in Figure 6b. The failure of the finite element model to buckle

Evolution of Inverse Opal Hydrogel Sensors

J. Phys. Chem. B, Vol. 110, No. 39, 2006 **19305**
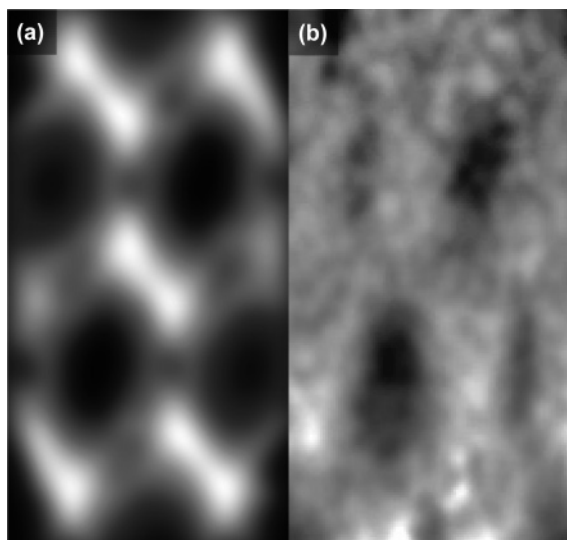
Figure 7. (a) Average of FCC(−110) finite element cross-sections between ±D/4 of the center of a pore. (b) FCC(−110) fluorescence image of hydrogel inverse opal (image taken from central region of Figure 5a, pH 5.7). The image has been flattened to account for the decrease in fluorescence intensity deeper into the sample; the substrate is at the bottom.

appears to be the root cause for the discrepancy between the model and the experimental system. Because the hydrogel is pinned on the substrate it can only expand in the substrate normal direction, resulting in a large strain energy. This strain, in the experimental system, is relaxed through buckling. The finite element model is built from a perfect coarse-grained mesh with no intrinsic instability, and thus does not buckle. Rather, it stores very high compressive strain energy within localized regions of the structure (Figure 6c,d), which leads to a loss of numerical accuracy. Because buckling is the reason for the FCC to L1$_1$ phase transformation, this phase transformation is not captured by the finite element model.

The model does much better simulating the FCC(−110) deformations. After the modeled deformations from different planes of the sample were averaged to approximate the focal volume collected in the microscope images, the predicted FCC-(−110) pore cross-sections (Figure 7a) match many of the features in the fluorescence images (Figure 7b). In particular, the alignment and interconnectivity of the pores are nicely simulated by the finite element model. The highly inhomogeneous strain and elongation of the pores normal to the substrate can be seen in both the fluorescence images and the finite element model.

Conclusions

We present the first direct observation of the structure of a responsive inverse opal hydrogel, and we compare the observed pore mesostructure evolution to the Bragg diffraction response and finite element analysis. From two different cross-sections of the distorted FCC mesostructure, we find that the pores appear to both elongate along the sample normal direction and collapse along the sample parallel directions, consistent with 1-D swelling of the interlayer distance. Interconnects between pores exhibit minimal deformation and act as anchor points to maintain a continuous aqueous phase. During expansion, the hydrogel lattice symmetry changes from FCC to L1$_1$. Reconstructed FCC-(−110) cross-sections confirm that a 1-D increase in the interlayer distance along the sample normal direction accounts

for the entire Bragg diffraction shift. Comparison with predictions from finite element modeling shows significantly greater deformation for the experimental hydrogel, particularly in the FCC(111) cross-sections, which may be due to inhomogeneous deformations and buckling driven by substrate pinning that are not captured by the finite element model.

References and Notes

(1) Asher, S. A.; Holtz, J.; Liu, L.; Wu, Z. J. *J. Am. Chem. Soc.* **1994**, *116*, 4997−4998.

(2) Holtz, J. H.; Asher, S. A. *Nature* **1997**, *389*, 829−832.

(3) Holtz, J. H.; Holtz, J. S. W.; Munro, C. H.; Asher, S. A. *Anal. Chem.* **1998**, *70*, 780−791.

(4) Lee, K.; Asher, S. A. *J. Am. Chem. Soc.* **2000**, *122*, 9534−9537.

(5) Asher, S. A.; Alexeev, V. L.; Goponenko, A. V.; Sharma, A. C.; Lednev, I. K.; Wilcox, C. S.; Finegold, D. N. *J. Am. Chem. Soc.* **2003**, *125*, 3322−3329.

(6) Alexeev, V. L.; Sharma, A. C.; Goponenko, A. V.; Das, S.; Lednev, I. K.; Wilcox, C. S.; Finegold, D. N.; Asher, S. A. *Anal. Chem.* **2003**, *75*, 2316−2323.

(7) Sharma, A. C.; Jana, T.; Kesavamoorthy, R.; Shi, L. J.; Virji, M. A.; Finegold, D. N.; Asher, S. A. *J. Am. Chem. Soc.* **2004**, *126*, 2971−2977.

(8) Hu, Z. B.; Lu, X. H.; Gao, J. *Adv. Mater.* **2001**, *13*, 1708−1712.

(9) Hu, Z. B.; Huang, G. *Angew. Chem., Int. Ed.* **2003**, *42*, 4799−4802.

(10) Debord, J. D.; Lyon, L. A. *J. Phys. Chem. B* **2000**, *104*, 6327−6331.

(11) Debord, S. B.; Lyon, L. A. *J. Phys. Chem. B* **2003**, *107*, 2927−2932.

(12) Takeoka, Y.; Watanabe, M. *Langmuir* **2002**, *18*, 5977−5980.

(13) Takeoka, Y.; Watanabe, M. *Langmuir* **2003**, *19*, 9104−9106.

(14) Lee, Y. J.; Braun, P. V. *Adv. Mater.* **2003**, *15*, 563.

(15) Lee, Y.-J.; Pruzinsky, S. A.; Braun, P. V. *Langmuir* **2004**, *20*, 3096−3106.

(16) Barry, R. A.; Wiltzius, P. *Langmuir* **2006**, *22*, 1369−1374.

(17) Hiltner, P. A.; Krieger, I. M. *J. Phys. Chem.* **1969**, *73*, 2386.

(18) Williams, R.; Crandall, R. S.; Wojtowicz, P. J. *Phys. Rev. Lett.* **1976**, *37*, 348.

(19) Clark, N. A.; Hurd, A. J.; Ackerson, B. J. *Nature* **1979**, *281*, 57.

(20) van Blaaderen, A.; Ruel, R.; Wiltzius, P. *Nature* **1997**, *385*, 321−324.

(21) Braun, P. V.; Zehner, R. W.; White, C. A.; Weldon, M. K.; Kloc, C.; Patel, S. S.; Wiltzius, P. *Adv. Mater.* **2001**, *13*, 721−724.

(22) Jiang, P.; Bertone, J. F.; Hwang, K. S.; Colvin, V. L. *Chem. Mater.* **1999**, *11*, 2132−2140.

(23) Vlasov, Y. A.; Bo, X. Z.; Sturm, J. C.; Norris, D. J. *Nature* **2001**, *414*, 289−293.

(24) Gu, Z. Z.; Fujishima, A.; Sato, O. *Chem. Mater.* **2002**, *14*, 760−765.

(25) Wong, S.; Kitaev, V.; Ozin, G. A. *J. Am. Chem. Soc.* **2003**, *125*, 15589−15598.

(26) Lu, Y.; Yin, Y. D.; Gates, B.; Xia, Y. N. *Langmuir* **2001**, *17*, 6344−6350.

(27) Hiltner, P. A.; Krieger, I. M. *J. Phys. Chem.* **1969**, *73*, 2386−2389.

(28) Tanaka, T.; Fillmore, D.; Sun, S.-T.; Nishio, I.; Swislow, G.; Shah, A. *Phys. Rev. Lett.* **1980**, *45*, 1636−1639.

(29) Katayama, S.; Hirokawa, Y.; Tanaka, T. *Macromolecules* **1984**, *17*, 2643−2645.

(30) Ilavsky, M.; Hrouz, J.; Ulbrich, K. *Polym. Bull.* **1982**, *7*, 107−113.

(31) Hirotsu, S. *J. Chem. Phys.* **1988**, *88*, 427−431.

(32) English, A. E.; Tanaka, T.; Edelman, E. R. *J. Chem. Phys.* **1997**, *107*, 1645−1654.

(33) Kikuchi, A.; Suzuki, K.; Okabayashi, O.; Hoshino, H.; Kataoka, K.; Sakurai, Y.; Okano, T. *Anal. Chem.* **1996**, *68*, 823−828.

(34) Miyata, T.; Asami, N.; Uragami, T. *Nature* **1999**, *399*, 766−769.

(35) Watanabe, M.; Akahoshi, T.; Tabata, Y.; Nakayama, D. *J. Am. Chem. Soc.* **1998**, *120*, 5577−5578.

(36) Anastase-Ravion, S.; Ding, Z.; Pelle, A.; Hoffman, A. S.; Letourneur, D. *J. Chromatogr., B* **2001**, *761*, 247−254.

(37) Walker, J. P.; Asher, S. A. *Anal. Chem.* **2005**, *77*, 1596.

(38) Mittleman, D. M.; Bertone, J. F.; Jiang, P.; Hwang, K. S.; Colvin, V. L. *J. Chem. Phys.* **1999**, *111*, 345−354.

(39) Brown, E. B.; Wu, E. S.; Zipfel, W.; Webb, W. W. *Biophys. J.* **1999**, *77*, 2837−2849.

(40) Van Keuren, E.; Schrof, W. *Macromolecules* **2003**, *36*, 5002−5007.

(41) Fergg, F.; Keil, F. J.; Quader, H. *Colloid Polym. Sci.* **2001**, *279*, 61−67.

(42) Booth, M. J.; Wilson, T. *J. Biomed. Opt.* **2001**, *6*, 266−272.

(43) Wakebe, T.; Van Keuren, E. *Jpn. J. Appl. Phys., Part 1* **1999**, *38*, 3556−3561.

(44) Perrin, D. D.; Dempsey, B. *Buffer for pH and Metal Ion Control*; Chapman and Hall Ltd.: London, 1974.

(45) Arruda, E. M.; Boyce, M. C. *J. Mech. Phys. Solids* **1993**, *41*, 389−412.

(46) Johnson, B.; Bauer, J. M.; Niedermaier, D. J.; Crone, W. C.; Beebe, D. J. *Exp. Mech.* **2004**, *44*, 21−28.

(47) Finel, A.; Mazauric, V.; Ducastelle, F. *Phys. Rev. Lett.* **1990**, *65*, 1016−1019.

(48) Itchkawitz, B. S.; McEllistrem, M.; Grube, H.; Boland, J. J. *Surf. Sci.* **1997**, *385*, 281−293.

(49) Song, Z. Y.; Hida, M.; Sakakibara, A.; Takemoto, Y. *Scr. Mater.* **1997**, *37*, 1617−1622.

(50) Wu, J. S.; Jia, C. L.; Urban, K.; Hao, J. H.; Xi, X. X. *J. Appl. Phys.* **2001**, *89*, 5653−5656.